

Article

Design, Modelling and Optimization of a High Power Density Axial Flux SRM with Reduced Torque Ripple for Electric Vehicles

Akbar Mohammadi Ajamloo ^{1,2}, Mohamed N. Ibrahim ^{1,2,3,*} and Peter Sergeant ^{1,2}

¹ Department of Electromechanical, Systems and Metal Engineering, Ghent University, 9000 Ghent, Belgium; akbar.mohammadiajamloo@ugent.be (A.M.A.); peter.sergeant@ugent.be (P.S.)

² FlandersMake@UGent—Corelab MIRO, 3001 Leuven, Belgium

³ Electrical Engineering Department, Kafrelshiekh University, Kafr el-Sheikh 33511, Egypt

* Correspondence: mohamed.ibrahim@ugent.be

Abstract: Switched reluctance machines (SRMs) are potential candidates for use in the propulsion systems of electric vehicles. However, they suffer from low power density and high torque ripple. In this paper, a segmented rotor double-sided axial flux SRM (DSAFSRM) is chosen for detailed analysis. A hybrid design algorithm is proposed to take the effects of iron non-linearity into account. The proposed design procedure benefits from simplicity and high accuracy at the same time. A two-step optimization procedure is presented which minimizes the torque ripple of the DSAFSRM without jeopardizing its efficiency. The torque ripple is reduced from 120% to 35% after optimization. In the two-step optimization procedure, both geometrical and switching related parameters are investigated. Moreover, a double-sided radial flux SRM is designed and compared with the proposed DSAFSRM in terms of torque ripple, average torque, efficiency and power density. The results indicate superior performance of the optimized DSAFSRM, especially in terms of average torque, which is 26% higher than the torque produced by the double-sided radial flux SRM.



Citation: Ajamloo, A.M.; Ibrahim, M.N.; Sergeant, P. Design, Modelling and Optimization of a High Power Density Axial Flux SRM with Reduced Torque Ripple for Electric Vehicles. *Machines* **2023**, *11*, 759. <https://doi.org/10.3390/machines11070759>

Academic Editors: Antonio J. Marques Cardoso, Payam Shams Ghahfarokhi, Ants Kallaste and Fan Wu

Received: 15 June 2023

Revised: 15 July 2023

Accepted: 18 July 2023

Published: 20 July 2023



Copyright: © 2023 by the authors. Licensee MDPI, Basel, Switzerland. This article is an open access article distributed under the terms and conditions of the Creative Commons Attribution (CC BY) license (<https://creativecommons.org/licenses/by/4.0/>).

Keywords: axial flux SRM; electric vehicle; hybrid design; magnetic equivalent circuit; segmented rotor; torque ripple

1. Introduction

Switched reluctance machines (SRMs) have drawn the attention of researchers for their potential use in the propulsion systems of electric vehicles (EVs). SRMs possess several merits compared with other electric machines, especially permanent magnet synchronous machines (PMSMs). A rare earth-free structure, wide power-speed range, simple structure and high durability are among the advantages of SRMs [1,2]. Consequently, SRMs have been designed to be used in a wide range of applications, namely, electric vehicles [3], electric bikes [4], electric aircraft [5], and wind turbines [6]. However, low power density and high torque ripple are serious drawbacks of this topology [7,8].

Excessive torque fluctuation can cause fatigue, mechanical failure, noise and vibration, which suggests the importance of torque ripple reduction in SRMs [9]. In [10], circular holes and a non-uniform air gap shape were employed to manipulate local saturation in the rotor and then minimize the torque ripple. Since iron saturation depends on the armature current, the optimization is only valid for a single working point rather than a wide working range. An overlapped winding scheme and rotor pole misalignment were proposed in [11], which considerably reduced the torque ripple. However, increased copper consumption and deteriorated efficiency were noted as consequences. In general, torque ripple suppression methods are categorized into two methods: geometry modifications and excitation regulations. The former method uses the following techniques: skewed rotor pole, pole offset, pole shifting, and rotor notch. These techniques have the following disadvantages:

performance degradation [12,13], increased manufacturing complexity [14,15], and being effective only in single working point [16,17]. Torque ripple reduction methods based on excitation regulations such as step current excitation control, modified direct torque control and hysteresis band-based torque sharing functions have been discussed in previous studies. Compared with geometrical methods, these techniques represent more promising improvements. However, they have some of the following drawbacks: increased switching loss [18], torque sensor requirement [19], complicated control logic [20,21], and excessive computational effort [22,23]. Therefore, an effective solution is proposed here which combines the advantages of both methods without imposing complexity and performance degradation.

In order to increase the power density of SRMs, several methods have been proposed in the literature, especially methods based on using PMs in SRM's structure [24–26]. However, this method may not justify replacement of PMSMs by SRMs since both topologies use rare earth materials. Employing a double-sided arrangement for radial flux SRMs was discussed in [27–29]. The solution is effective due to the increased air gap surface area but has the disadvantages of complex mechanical structure, uneven distribution of power between stators and a complicated cooling system. In order to overcome these problems while maintaining high power density, segmented rotor double-sided axial flux SRMs (DSAFSRM) could be considered as a suitable topology [30].

Several topologies of segmented rotor DSAFSRMs have been discussed, which may be categorized in three configurations, as in Figure 1. Double-rotor single-stator AFSRM topology is depicted in Figure 1a. In this topology, the stator is sandwiched between two rotor disks and the rotor is composed of separate iron segments fixed by a non-magnetic holder. The double-rotor single-stator AFSRM has the advantage of low copper loss and high efficiency due to small winding overhang [31,32]. However, heat dissipation from the stator is difficult due to the small contact area between the stator and the surrounding air. A configuration of a DSAFSRM with two stators and one rotor is depicted in Figure 1b. In this topology, two stators are located on two ends of the motor and a segmented rotor is placed in the middle [33,34]. In contrast to the previous topology, this topology offers good thermal behavior due to large contact area between the stators and the surroundings. Another DSAFSRM topology called the Pancake structure is depicted in Figure 1c. As can be seen, the stator and rotor have a segmented structure which yields a lightweight structure [35,36]. The Pancake topology produces a high power density, but its mechanical integrity and reliability are questionable.

Standard design formulations for DSAFSRMs were presented in [37,38]. However, the design procedures did not take the effect of leakage flux and magnetic non-linearity into account. In [39], a design process based on a 3-D finite element method (FEM) was presented which showed a high level of accuracy but required intensive computational time. A coupled analytical-numerical design procedure for an AFSRM was discussed in [40]. The machine's design equations were derived and coupled to the 3-D FEM to take the effect of fringing flux and iron saturation into account. Nevertheless, the proposed algorithm suffered from high computational time and low robustness. In [41], a design algorithm for AFSRMs was proposed where classical equations and the magnetic equivalent circuit (MEC) method were combined. In the design procedure, the effects of fringing and leakage flux were considered by the MEC method. However, non-linearity of the magnetic materials was not taken into account, which reduced accuracy of the method.

The contributions of this paper are as follows: (1) a proposed hybrid design algorithm based on a non-linear MEC model and classical formulations of the DSAFSRM; (2) a two-step torque ripple minimization solution based on optimization of switching and geometrical parameters; and (3) a comparative study of double-sided SRMs with axial and radial flux configurations. In Section 2, the hybrid design procedure and its non-linear algorithm are presented. In Section 3, the performance of the designed DSAFSRM is addressed, and the two-step torque ripple suppression method is discussed in Section 4. In Section 5, the optimized machine is compared with a double-sided radial flux SRM under the same constraints to evaluate their performance and the effectiveness of the proposed methods.

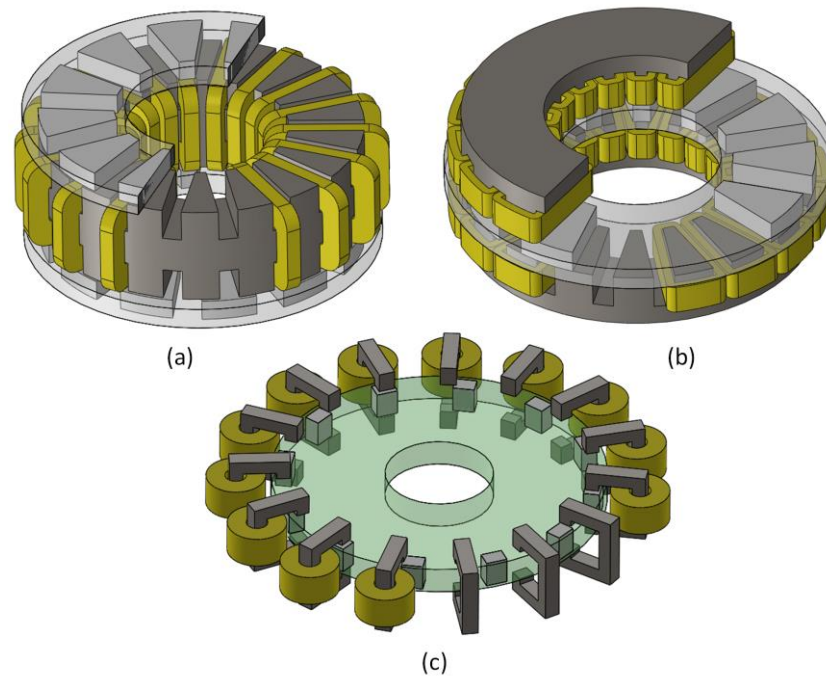


Figure 1. Configurations of segment rotor double-sided axial flux SRMs. (a) Single-stator and double-rotor topology. (b) Double-stator and single-rotor topology. (c) Pancake topology.

2. Hybrid Design Procedure for the DSAFSRM

In this section, a hybrid design procedure for the DSAFSRM shown in Figure 1b is proposed. The design algorithm employs DSAFSRM's analytical equations along with non-linear MEC to take the effects of iron non-linearity and leakage flux into account. In this regard, the proposed algorithm simultaneously benefits from low computational effort and a high level of accuracy.

2.1. DSAFSRM's Design Equations

The flux linkage equation of the motor can be written as in (1) [42]:

$$V_{dc} - R_{ph}i_{(t)} = \partial\lambda_{ph}/\partial t \quad (1)$$

where V_{dc} is the dc link voltage, and R_{ph} and λ_{ph} are the wire resistance and flux linkage per phase, respectively. It should be noted that (1) applies to the period of time when the rotor moves from the unaligned to aligned position and $i_{(t)}$ reaches to its peak value (I), which is assumed constant. By neglecting the phase resistance, it can be re-written as in (2) [42]:

$$V_{dc} = \partial\lambda_{ph}/\partial t = \frac{(L_a^{sat} - L_u)}{T} I \quad (2)$$

where L_a^{sat} and L_u are saturated aligned and unaligned phase inductances, respectively. T is the period of time when the rotor moves from the unaligned to aligned position and can be calculated as in (3).

$$T = \beta_s / \omega_m \quad (3)$$

where ω_m is the rotor angular velocity and β_s is the stator pole shoe angle. The variable K_L is defined as the ratio of unaligned inductance to saturated aligned inductance as in (4).

$$K_L = \frac{L_u}{L_a^{sat}} \quad (4)$$

Then, by applying (3) and (4) into (2), the voltage equation can be written as follows [42]:

$$V = L_a^{sat} I \frac{\omega_m}{\beta_s} (1 - K_L) \quad (5)$$

At the aligned position, the flux linkage equation can be written as in (6).

$$L_a^{sat} I = N_{ph} \varphi_{ph} = N_{ph} B_{pole} A_{pole} \quad (6)$$

where N_{ph} is the coil turn per phase, and B_{pole} and A_{pole} are the average magnetic flux density and area, respectively, of one stator pole. The stator pole area (A_{pole}) can be calculated as in (7).

$$A_{pole} = \frac{\beta_s}{8} (D_o^2 - D_i^2) = \frac{\beta_s D_o^2}{8} (1 - K_s^2) \quad (7)$$

D_o and D_i are the outer and inner diameters, respectively, of the stator disk, and K_s is the ratio of the inner diameter to the outer diameter. Thus, (6) can be re-written as in (8).

$$L_a^{sat} I = \frac{N_{ph} \beta_s B_{pole}}{8} D_o^2 (1 - K_s^2) \quad (8)$$

The electrical loading and output power of the double-stator AFSRM are written as (9) and (10), respectively.

$$A_m = \frac{2N_{ph} I}{\pi(D_o + D_i)/2} = \frac{4N_{ph} I}{\pi D_o (1 + K_s)} \quad (9)$$

$$P_o = \eta K_d V_{dc} I \quad (10)$$

where η is the efficiency, and K_d is the ratio of the actual duty cycle of the phase current to its maximum allowable duty cycle, which is calculated as in (11).

$$K_d = \frac{2N_r \alpha}{360} \quad (11)$$

N_r is the number of rotor poles, and α is the actual conduction angle in each stroke. Finally, the combination of (5), (8), (9) and (10) yields the output power of the double-stator single-rotor AFSRM.

$$P_o = \frac{\pi^2 \eta K_d (1 - K_L)}{960} B_{pole} A_m n_m D_o^3 (1 - K_s^2) (1 + K_s) \quad (12)$$

It should be noted that n_m is the mechanical speed of the rotor in rpm. The above equation can be rearranged to calculate the outer diameter of the DSAFSRM:

$$D_o = \sqrt[3]{\frac{960 P_o}{\pi^2 \eta K_d (1 - K_L) B_{pole} A_m n_m (1 - K_s^2) (1 + K_s)}} \quad (13)$$

As the above formulation indicates, calculation of the outer diameter requires the values of input parameters (output power, speed, magnetic and electrical loadings) and initializing the remaining parameters. This leads to an iterative algorithm which will be discussed later. Using the previously discussed electrical loading calculated in Equation (9), the number of winding turns per phase is calculated:

$$N_{ph} = \frac{\pi D_o (1 + K_s) A_m}{8 I} \quad (14)$$

The wire diameter is calculated based on the assumed value for current density (δ) and the stator rms current (I_{rms}):

$$d_w = \sqrt{\frac{4S_w}{\pi}} = \sqrt{\frac{4I_{rms}}{\pi\delta}} \quad (15)$$

Next, the stator slot area is calculated:

$$S_{slot} = \frac{mN_{ph}S_w}{N_s F_f} \quad (16)$$

where m , S_w and F_f are the number of phases, wire cross-sectional area and slot fill factor, respectively. By choosing rectangular stator slots, the slot opening (W_{so}) and slot height (d_{sh}) can be determined by the following formulations.

$$W_{so} = \left(\frac{2\pi}{N_s} - \beta_s\right)(D_o + D_i)/4, \quad d_{sh} = \frac{S_{slot}}{W_{so}} \quad (17)$$

The conductor length per phase, phase resistance and copper loss can be then calculated using (18)–(20), respectively [43].

$$L_{wire} \approx N_{ph} \left[1.1(D_o - D_i) + \frac{\pi}{N_s}(D_o + D_i)\right] \quad (18)$$

$$R_{ph(\theta)} = L_{wire} r_w [1 + \alpha(\theta - 20)] \quad (19)$$

$$P_{cu} = m R_{ph(\theta)} I_{rms}^2 \quad (20)$$

where r_w , α and θ are the conductor resistance per meter at 20 °C, resistance coefficient, and working temperature, respectively.

The accuracy of the above-mentioned design procedure is highly influenced by the ratio of unaligned inductance to saturated aligned inductance (K_L in (4)). This signifies the need for a complementary approach to increase the accuracy of the design procedure without imposing considerable complexity and computational effort. To do so, a non-linear MEC is developed in the next section and then combined with the classical equations, leading to a hybrid design procedure.

2.2. Non-Linear MEC

Since the factor K_L is very sensitive to iron saturation level and the machine's detailed geometry, it is not possible to calculate it using classical formulations. In this section, a non-linear MEC is developed to calculate the value of K_L , leading to a more accurate analytical design procedure. The MEC is only established at unaligned and aligned positions of the rotor since the value of K_L is solely dependent on these two positions.

2.2.1. Permeance Network

The permeance network of the DSAFSRM at the aligned and unaligned positions is depicted in Figure 2. In order to take the effect of iron saturation into account, non-linear permeances are adopted for the iron parts placed on the main flux path highlighted in red. Owing to machine's symmetry, the permeance networks at the aligned and unaligned positions are reduced to circuits, as shown in Figure 2b,d, respectively.

The permeance networks shown in Figure 2b,d can be solved based on the following formulation [44]:

$$[G] \times [V] = [\phi] \quad (21)$$

where G , V and Φ are the permeance, node potential and flux matrix whose expanded forms are given in Appendix A.

The magnetic potential ($V_i, i = 1, 2, 3, \dots$) at all nodes is determined by solving the network. Then, the flux generated by the active phase can be calculated as in (22).

$$\varphi_a = G_{t1}(V_1 + N_c I_a) \tag{22}$$

When the magnetic fluxes associated with the aligned and unaligned positions are determined, K_L is simply calculated as in (23).

$$K_L = \frac{\varphi_a^{unaligned}}{\varphi_a^{aligned}} \tag{23}$$

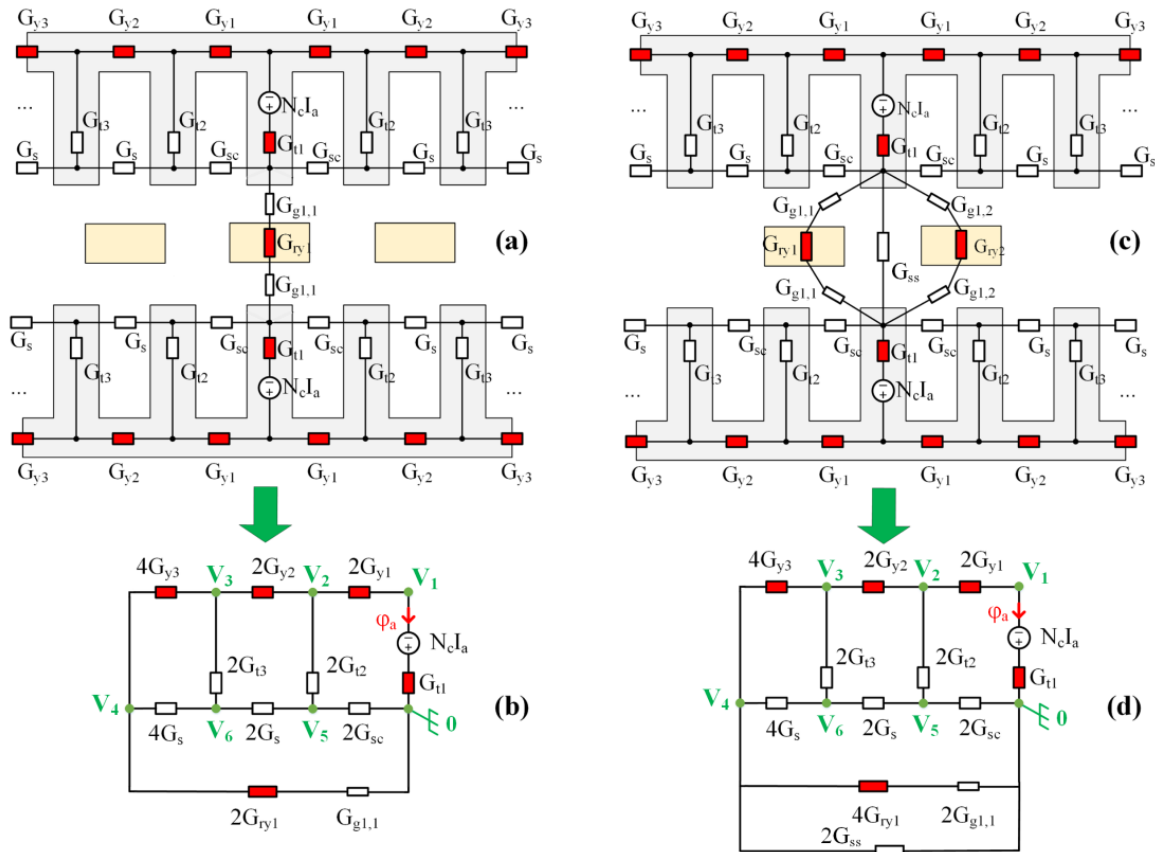


Figure 2. Non-linear permeance network of the DSAFSRM (non-linear permeances highlighted in red). (a) Full model at aligned position. (b) Reduced model at aligned position. (c) Full model at unaligned position. (d) Reduced model at unaligned position.

2.2.2. Air Gap Permeances

Precise calculation of air gap permeances is the key to developing an accurate MEC. In this regard, the permeances between the rotor and stator at aligned and unaligned positions are investigated here. To do so, it is seen in Figure 3a that there are three types of flux tubes between the rotor and stator at the aligned position. The first flux tube (FT_0) is associated with the front surfaces of rotor and stator whose corresponding permeance can be calculated as in (24).

$$G_{FT0} = 0.5\mu_0(D_o - D_i) \int_0^{W_{st}} \frac{dx_0}{L_g} = \frac{\mu_0 W_{st} (D_o - D_i)}{2L_g} \tag{24}$$

Flux tube FT_1 is associated with the rotor's front surface and stator's side surface. This flux tube consists of a straight line and a curved line, which for simplicity, is assumed to be a circular curve. The permeance associated with this flux tube is calculated as in (25).

$$G_{FT1} = 0.5\mu_0(D_o - D_i) \int_0^{(W_{rt}-W_{st})/2} \frac{dx_1}{L_g + 0.5\pi x_1} = \frac{\mu_0(D_o - D_i)}{\pi} Ln[1 + \pi(W_{rt} - W_{st})/4L_g] \quad (25)$$

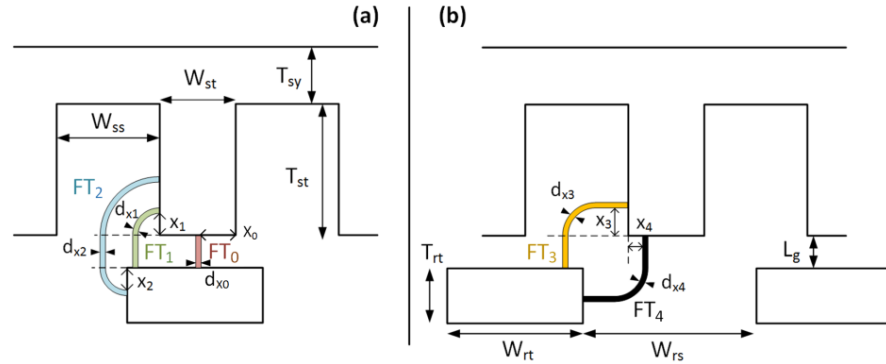


Figure 3. Parametric dimensions of the DSAFSRM and air gap flux tubes. (a) Aligned position. (b) Unaligned position.

With regard to the aligned position, the third flux tube (FT_2) is related to the side surfaces of the stator and rotor. As can be seen from Figure 3a, FT_2 is composed of two curved paths and one straight path whose corresponding permeances are calculated as in (26).

$$G_{FT2} = 0.5\mu_0(D_o - D_i) \int_0^{T_{rt}} \frac{dx_2}{L_g + \pi[(W_{rt} - W_{st})/4 + x_2]} = \frac{\mu_0(D_o - D_i)}{2\pi} Ln[1 + \frac{4\pi T_{rt}}{4L_g + \pi(W_{rt} - W_{st})}] \quad (26)$$

Consequently, the air gap permeance between the rotor and stator poles at the aligned position is calculated by the following equation:

$$G_{g1,1}^{aligned} = G_{FT0} + 2G_{FT1} + 2G_{FT2} \quad (27)$$

As can be seen in Figure 3b, two types of flux tubes are considered between the rotor and stator at the unaligned position. FT_3 and FT_4 are comprised of two straight lines and a circular curve which relate a side surface to a front surface. The corresponding permeances of FT_3 and FT_4 are written as in (28) and (29).

$$G_{FT3} = 0.5\mu_0(D_o - D_i) \int_0^{(W_{rt}-W_{st})/2} \frac{dx_3}{L_g + 0.5[(W_{rs} - W_{st}) + \pi x_3]} = \frac{\mu_0(D_o - D_i)}{\pi} Ln[1 + \frac{W_{rt} - W_{st}}{4L_g + 2(W_{rs} - W_{st})}] \quad (28)$$

$$G_{FT4} = 0.5\mu_0(D_o - D_i) \int_0^{\min(T_{rt}, W_{st})} \frac{dx_4}{L_g + 0.5[(W_{rs} - W_{st}) + \pi x_4]} = \frac{\mu_0(D_o - D_i)}{\pi} Ln[1 + \frac{\min(T_{rt}, W_{st})}{4L_g + 2(W_{rs} - W_{st})}] \quad (29)$$

After obtaining the permeance values corresponding to FT_3 and FT_4 , the air gap permeance between the rotor and stator poles at the unaligned position is calculated as in (30).

$$G_{g1,1}^{unaligned} = G_{FT3} + G_{FT4} \quad (30)$$

The permeance between two stator poles, which is represented by G_{ss} in Figure 2b, is calculated as in (31).

$$G_{ss} = \frac{0.5\mu_0 W_{st}(D_o - D_i)}{2L_g + T_{rt}} \quad (31)$$

The stator slots are categorized as slots with and without current-carrying conductors. In this regard, G_{sc} and G_s , which are air gap permeances associated with the current-carrying and non-current-carrying slots, respectively, are calculated as follows.

$$G_{sc} = \frac{\mu_0 T_{st}(D_o - D_i)}{4W_{ss}}, \quad G_s = 2G_{sc} \quad (32)$$

2.2.3. Non-Linear Hybrid Algorithm

Accurate calculation of K_L requires taking the iron saturation effect into account. In this regard, permeances positioned on the main flux path (highlighted in red in Figure 2) are considered to be non-linear. They are subjected to a considerable amount of magnetic saturation, especially at the aligned position. It should be mentioned that the stator teeth without a magneto motive force (MMF) source are not subjected to saturation. Therefore, their corresponding permeances are considered linear (i.e., G_{t2} , G_{t3}). The equations associated with the iron part permeances are given in (33).

$$G_{t1} = \frac{\mu_{t1}W_{st}(D_o - D_i)}{2T_{st} + T_{sy}}, \quad G_{y1} = \frac{\mu_{y1}T_{sy}(D_o - D_i)}{2(W_{st} + W_{ss})}, \quad (33)$$

where μ_{t1} and μ_{y1} are the permeabilities of the aligned stator tooth and its adjacent yoke, respectively.

The proposed algorithm of the hybrid method is presented in Figure 4 in which steps associated with the classical and MEC methods are depicted in distinct colors. In the beginning, the DSAFSRM's ratings and main specifications such as power, speed, pole number, etc., are imported. Next, K_L and efficiency (η) are initialized, which is followed by obtaining the machine's dimensions and electrical parameters using the classical formulations (10)–(20). At this stage, the algorithm moves to the MEC section by developing DSAFSRM's permeance network. Next, the permeances associated with air gap and linear iron parts are calculated. In order to determine the permeability of the saturated parts, a function is fitted on the B - H curve of the iron. Then, B and H values are calculated using an iterative algorithm. Thus, the non-linear permeances are calculated and the permeance network is solved using (21, Appendix A). Next, K_L is calculated and compared with its initial value. If the assumed values for K_L and η match their initial values, the algorithm finishes; otherwise, it returns to the step in which the two parameters are initialized.

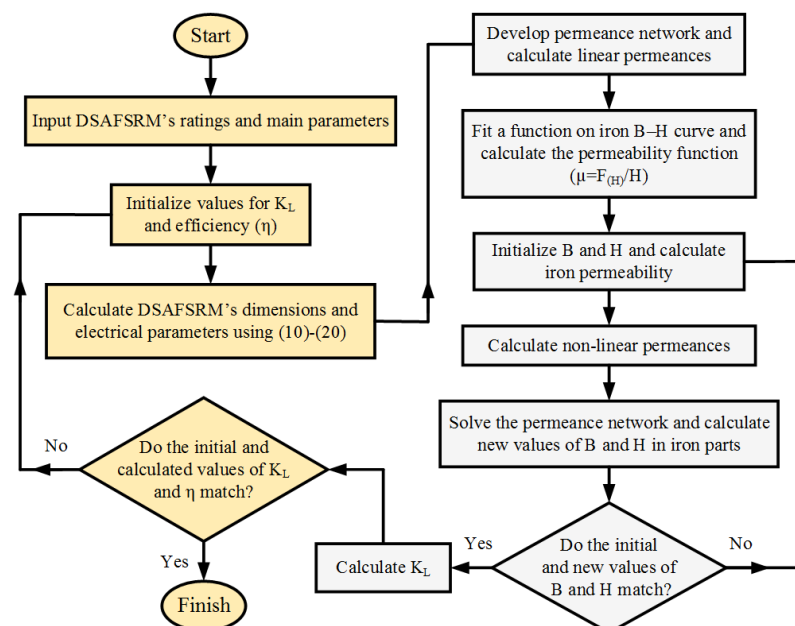


Figure 4. Non-linear algorithm of the proposed hybrid design procedure.

3. Electromagnetic Performance Analysis

In this section, the electromagnetic performance of the designed DSAFSRM is discussed. The DSAFSRM is designed with a rated power of 100 kW at 3000 rpm, and further specifications are listed in Table 1. The detailed analysis and optimization steps are performed using finite element analysis (FEA). In the FEA environment, 2-D geometry is used instead of 3-D, which has the advantages of reduced mesh elements, tolerable processing time and an acceptable level of accuracy. Additionally, only 1/6th of the full model is used rather than the whole model, resulting in a considerably reduced number of mesh elements, as shown in Figure 5.

Table 1. Main specifications of the designed DSAFSRM.

| Parameter | Symbol | Value |
|------------------------------|----------|-------|
| Output power (kW) | P_o | 100 |
| Nominal speed (rpm) | n_m | 3000 |
| DC link voltage (V) | V_{dc} | 440 |
| Outer diameter (mm) | D_o | 370 |
| Inner diameter (mm) | D_i | 148 |
| Active length (mm) | L_m | 111 |
| Number of stator poles | N_s | 18 |
| Number of rotor poles | N_r | 12 |
| Air gap length per side (mm) | L_g | 0.5 |
| Number of turns per coil | N_c | 5 |
| Stator slot opening (mm) | W_{ss} | 20 |
| Stator slot depth (mm) | T_{st} | 28 |
| Stator yoke thickness | T_{sy} | 18 |
| Rotor length | T_{rt} | 18 |
| Slot fill factor | F_f | 50 |

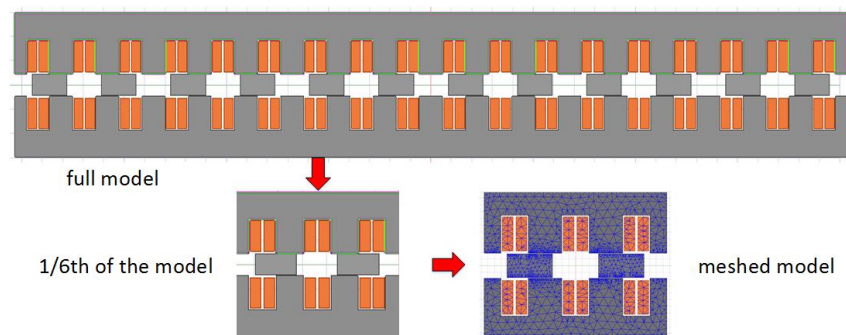


Figure 5. 2-D structure of the designed DSAFSRM in the FEA environment.

A vector plot of the magnetic flux density distribution in the AFSRM is depicted in Figure 6 at the unaligned and aligned positions. A nominal peak current of 320 A is injected into phase A, and it can be observed that the flux density at the aligned position is approximately 1.8 T in the stator pole and roughly 1.3 T in the stator yoke. The flux linkage profile of the designed AFSRM is extracted at different rotor positions and presented in Figure 7. It can be seen that at the unaligned position (0°) the flux linkage has the minimum value of 0.08 Wb due to experiencing the largest air gap reluctance on the main flux path. In contrast, the flux linkage profile at the aligned position (15°) reaches 0.3 Wb and becomes saturated by saturation of the stator poles (Figure 6b).

The instantaneous electromagnetic torque produced by phase A is presented in Figure 7 for different rotor positions at 320 A current. It can be seen that the static torque starts from zero at the unaligned position (0°) and reaches its maximum value. When the rotor pole reaches perfect alignment with the stator pole (15°), the reluctance of the main flux path reaches a minimum and the electromagnetic torque becomes zero. With further movement of the rotor, the reluctance increases and a negative torque is produced

to keep the rotor in alignment with the stator (keeping the reluctance at a minimum value). Thus, in order to produce positive torque, the maximum conduction period in each conduction period should not exceed $180^\circ/N_r$. In the case of the 18/12 DSAFSRM, the conduction period should not exceed 15° . However, due to the machine's large inductance, the current would not immediately fall to zero after reaching the aligned position, which results in negative torque production. Consequently, the phase switches should be turned off at some point before reaching the aligned position. In this regard, it is convenient to take the conduction angle as $360^\circ/mN_r$, where m is the number of phases. Thus, the conduction angle would be 10° in the DSAFSRM under study.

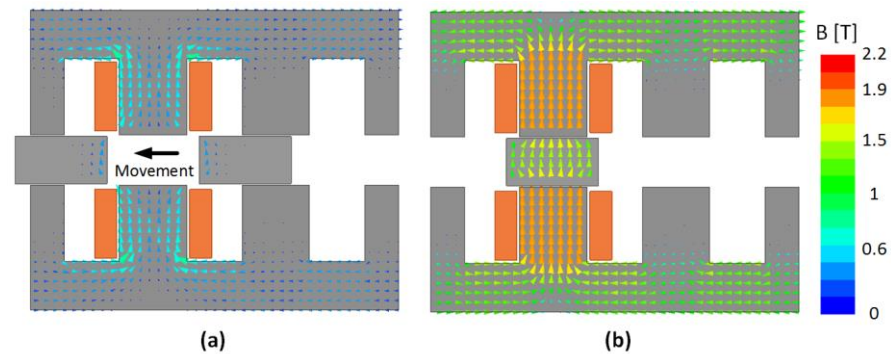


Figure 6. Vector plot of the magnetic flux density distribution in the DSAFSRM at the rated current. (a) Unaligned position. (b) Aligned position.

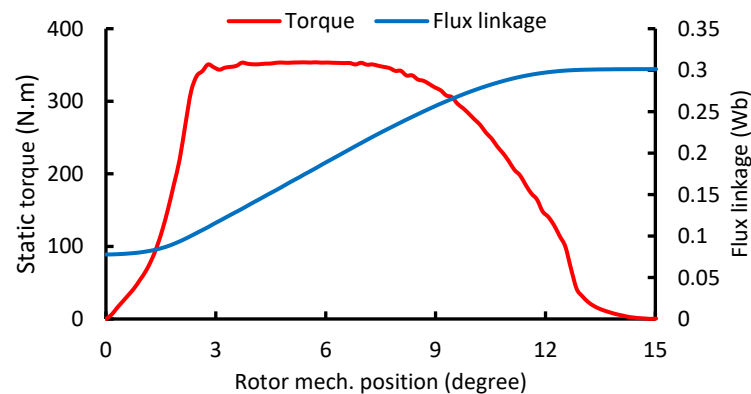


Figure 7. Flux linkage and static torque versus rotor position of the DSAFSRM.

4. Torque Ripple Minimization

In this section, torque ripple minimization of the DSAFSRM under study is addressed. High levels of torque ripple are an intrinsic drawback of SRMs and this poses serious challenges to their application, especially in EV powertrains. A high level of torque ripple results in excessive noise and vibration, causes damage to ball bearings and the shaft, and reduces the reliability of the powertrain. In this regard, two torque ripple minimization approaches relying on conventional and proposed methods are discussed here.

4.1. Conventional Pole Coverage Optimization

In SRMs, the torque ripple level is sensitive to the stator and rotor pole coverage. Therefore, sensitivity analysis can be performed to find the optimum values for these two parameters. Here, B_s and B_r are the stator pole and rotor pole coverage, respectively, which are defined as the ratio of the pole shoe to their corresponding pole pitch. In this regard, the results of the sensitivity analysis are presented in Figure 8. As can be seen, the DSAFSRM's torque ripple is influenced by these two parameters fluctuating between 115% and 130%. However, this range of torque ripple cannot be tolerated in many applications, including

in EV powertrains. Consequently, alternative methods should be adopted to effectively reduce the torque ripple of the DSAFSRM.

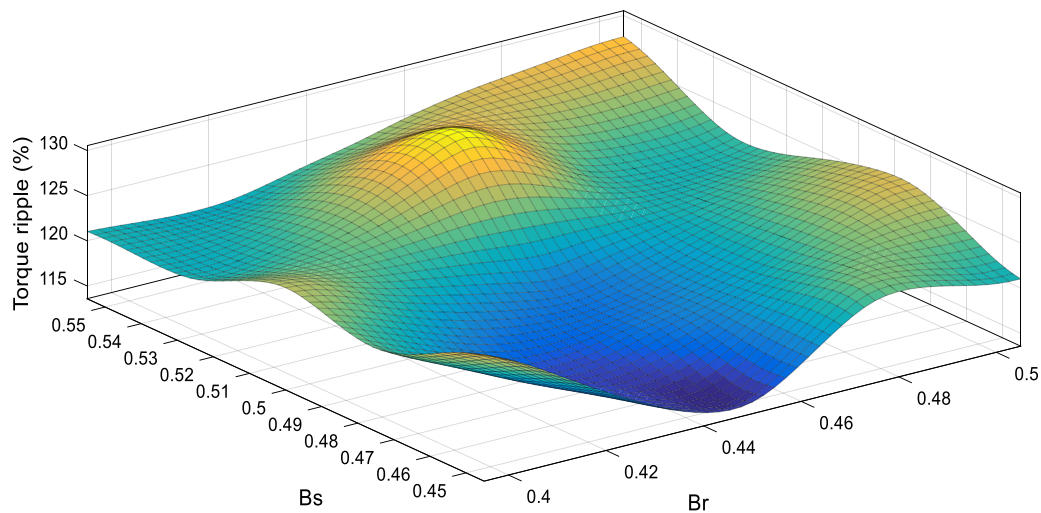


Figure 8. Surface plot of torque ripple versus stator and rotor pole coverage using the conventional optimization method.

4.2. Proposed Two-Step Optimization

To develop an effective solution for torque ripple minimization, a two-step sensitivity analysis is suggested in this paper. In the proposed method, the switching parameters and pole coverage are optimized in separate layers.

In the first layer, the advanced switching angle and extended switching period are analyzed as two important variables. After finding the optimum value for these two parameters, a sensitivity analysis is again carried out to find optimum values for the stator and rotor pole coverage. In this regard, two switching parameters are taken as optimization variables. The first variable “*a*” is defined as the advanced firing angle. This parameter determines how soon the phase switches should be turned on before the rotor reaches the unaligned position. The second variable “*b*” is defined as the extended switching period. Since in the DSAFSRM, each conduction period is 10° , “*b*” has a value greater than 10° . The result of the first layer optimization is presented in Figure 9. It can be seen that varying these two parameters has a considerable effect on the torque ripple. The torque ripple can be reduced to minimum value of 42% by selecting $a = 2^\circ$ and $b = 13^\circ$.

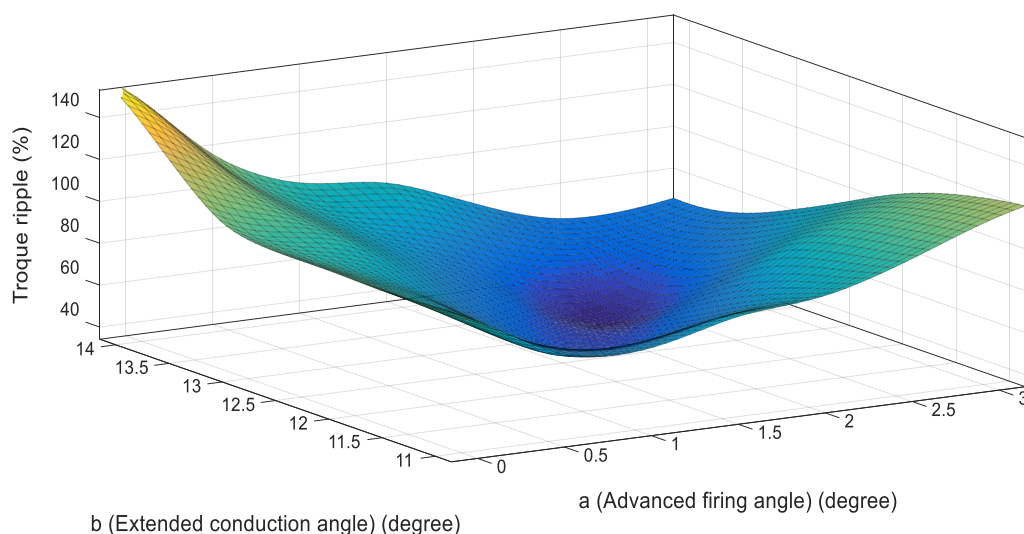


Figure 9. Surface plot of torque ripple versus conduction and firing angles.

In the second layer of the optimization process, different stator and rotor pole coverage (B_s and B_r) are evaluated when a and b are fixed at their optimum values. In this regard, the torque ripple versus B_s and B_r is shown in Figure 10. It can be seen that the torque ripple is very sensitive to variations in B_s and B_r , fluctuating between 35% and 75%. Selecting $(B_s, B_r) = (0.525, 0.5)$ and/or $(B_s, B_r) = (0.5, 0.525)$ would yield the minimum torque ripple (35%). Examining the DSAFSRM's efficiency versus B_s and B_r in Figure 11 can determine the most suitable combination. It can be seen that the efficiency is greatly affected by the rotor pole coverage (B_r) rather than B_s . It is also understood that the relationship between efficiency and B_r is inverse linear, where higher B_r results in lower efficiency. Consequently, $(B_s, B_r) = (0.525, 0.5)$ would be a better choice since it yields the minimum torque ripple at a higher efficiency value.

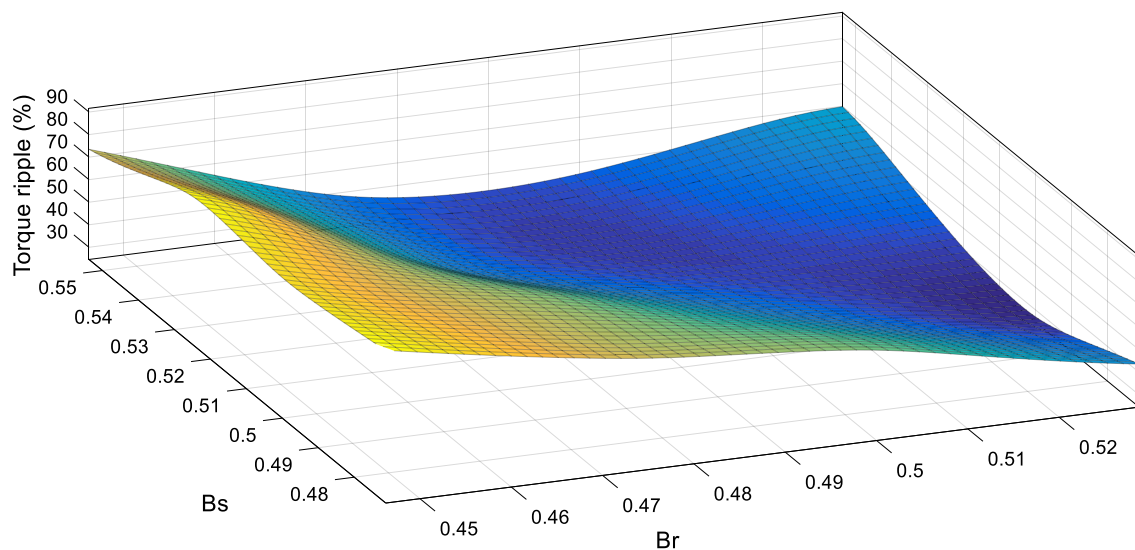


Figure 10. Surface plot of torque ripple versus stator and rotor pole coverage using the double-layer optimization method.

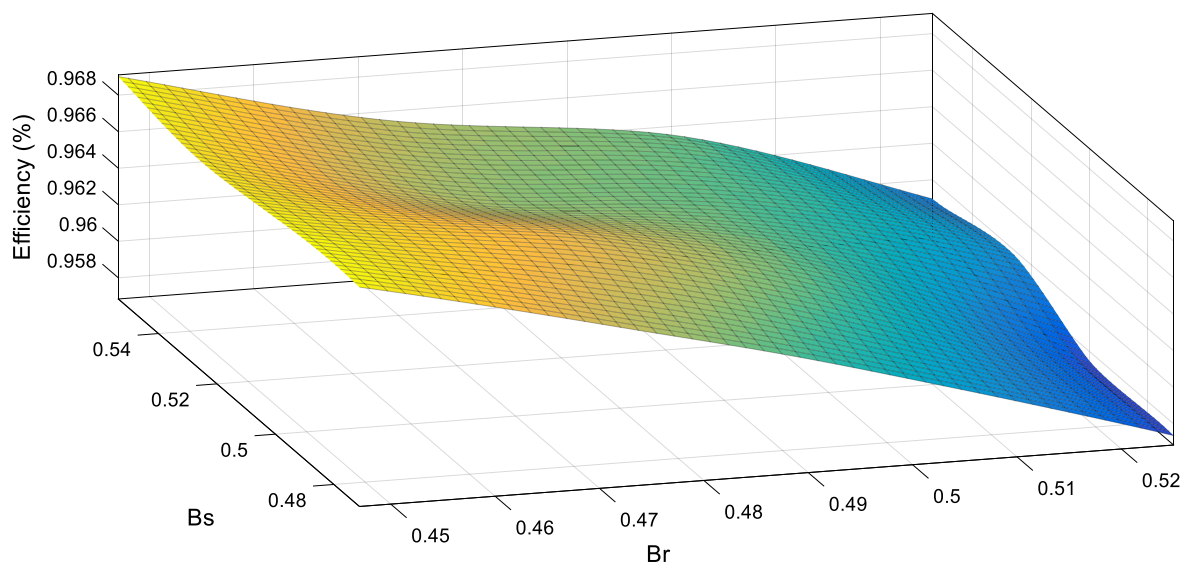


Figure 11. Surface plot of DSAFSRM's efficiency versus stator and rotor pole coverage.

5. Comparative Analysis

In the previous sections, the design, modelling and optimization of the DSAFSRM have been discussed. In order to have better insight into performance of the optimized DSAFSRM, a comparative study is also conducted. In this regard, an 18/12 double-sided radial flux SRM

is designed with the same speed, diameter, length and current density as the DSAFSRM. The radial flux SRM has a double-stator arrangement and a segmented rotor configuration in the middle. In practice, rotor segments are fixed using a non-magnetic material to guarantee integrity of the rotor without increasing flux leakage between the segments.

The flux density distribution in the radial flux SRM in the aligned and unaligned positions is depicted in Figure 12. It can be seen that at the aligned position, the flux density in the yoke region is around 1.3 T where no saturation occurs. However, close examination of the stator pole region reveals that the flux density in the outer and inner stator poles reaches up to 1.8 T and 1.95 T, respectively. The uneven distribution of flux density in the stator poles is due to the smaller dimensions of the inner stator with respect to the outer one, which is not avoidable in this topology. Consequently, the inner stator poles become more saturated than the outer stator poles, resulting in non-efficient use of the machine's material and volume. The opposite pattern is observed in the DSAFSRM, where flux density distribution in the stators is identical (Figure 6). Therefore, both stators become saturated at the same time, resulting in a more efficient use of material and volume.

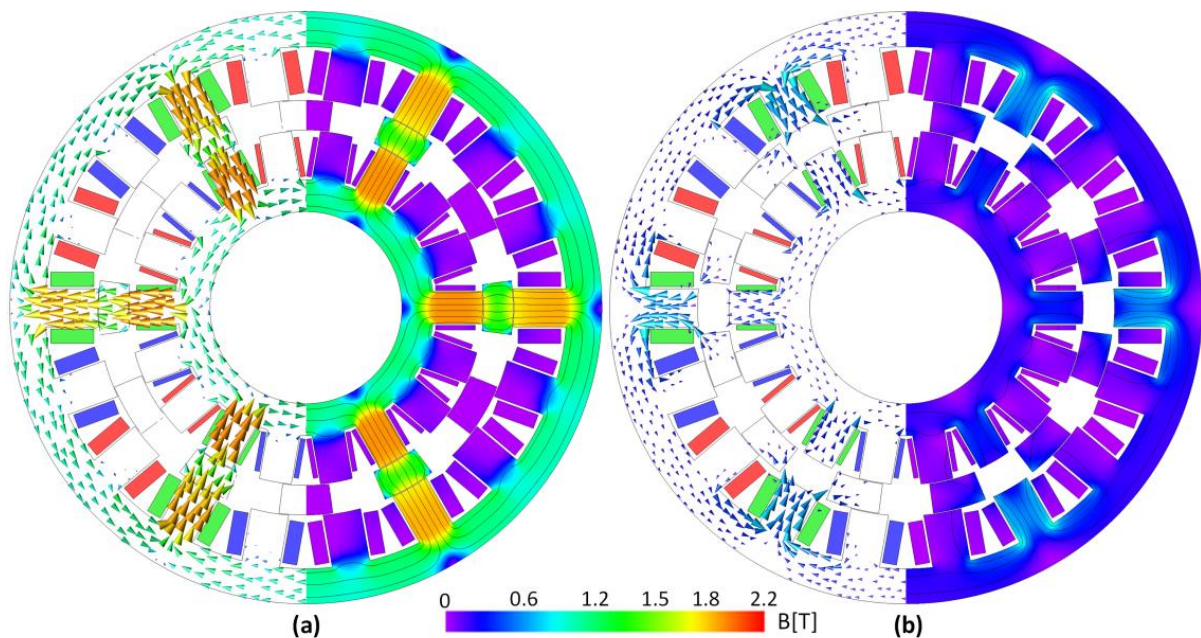


Figure 12. Magnetic flux density distribution in the double-sided radial flux topology at rated current. (a) Aligned position. (b) Unaligned position.

In order to gain better insight into the different performance of the two topologies, flux linkage versus armature current is extracted and depicted in Figure 13. It can be seen that the area trapped between the aligned and unaligned curves of the DSAFSRM is larger than the area corresponding to the double-sided radial flux SRM. Since this area is proportional to the converted energy in one cycle, the DSAFSRM has a potentially higher power rating than its radial flux counterpart. Next, a full load torque profile of the DSAFSRM is extracted before and after optimization and compared with the double-sided radial flux SRM in Figure 14. It is seen that the average torque of the DSAFSRM and radial flux SRM are approximately 318 N m and 253 N m, respectively. It is noteworthy that the average torque of the DSAFSRM remains roughly unchanged after the optimization process. Furthermore, the torque ripple of the non-optimized DSAFSRM and radial flux SRM are roughly 120% and 92%, respectively. It can also be seen that the torque ripple of the DSAFSRM falls dramatically to approximately 35% after the optimization process.

The main specifications of the DSAFSRM (before and after optimization) and the double-sided radial flux SRM are listed in Table 2. It can be seen that speed, current density, volume and air gap length of all three machines are equal. It is clear that the

optimized DSAFSRM has the highest power rating of 100 kW, while the power rating of the radial flux SRM is only 79.5 kW. There may be two important explanations for this issue: (1) The air gap surface area of the DSAFSRM in which the energy conversion takes place is larger than its radial flux counterpart. The DSAFSRM benefits from two identical air gap surfaces, while the radial flux SRM has two uneven air gap surfaces which provide a smaller area for energy conversion. (2) Due to non-identical stators of the radial flux SRM, the magnetic reluctance of the main flux path is chiefly determined by the smaller stator. Consequently, the volume and mass utilization in the radial flux SRM is less efficient than in the DSAFSRM, leading to a lower power rating in the same space. According to Table 2, the efficiency of the DSAFSRM increases by 0.2% after optimization. At the same time, owing to the proposed optimization process, the torque fluctuation of the DSAFSRM has dropped by 85%. Among the three machines, the optimized DSAFSRM represents the highest power density (8.38 N m/cm^3), while the double-sided radial flux SRM has the lowest power density (6.66 N m/cm^3).

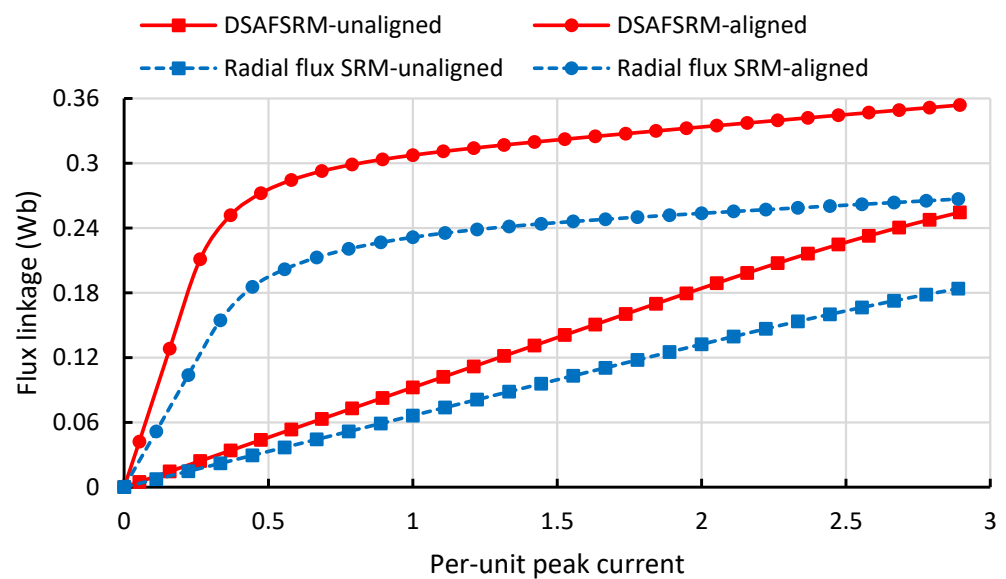


Figure 13. Flux linkage versus armature current of the DSAFSRM and radial flux SRM at aligned and unaligned position.

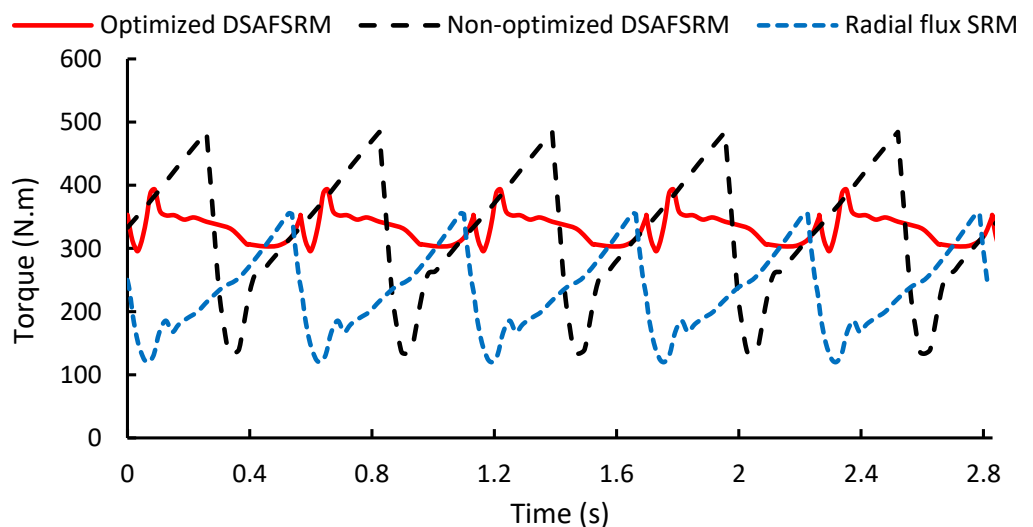


Figure 14. Full-load torque profile of the radial flux SRM and the proposed DSAFSRM before and after optimization.

Table 2. Main parameters of the DSAFSRMs and the double-sided radial flux SRM.

| Parameter | Optimized DSAFSRM | Non-Optimized DSAFSRM | Double-Sided Radial Flux SRM |
|--------------------------------------|-------------------|-----------------------|------------------------------|
| Rated speed (rpm) | | 3000 | |
| Outer diameter (mm) | | 370 | |
| Active length (mm) | | 111 | |
| Current density (A/mm ²) | | 8 | |
| Air gap length (mm) | | 0.5 | |
| Output power (kW) | 100 | 99.7 | 79.5 |
| Copper loss (kW) | 2.4 | 2.3 | 2.1 |
| Core loss (kW) | 1.5 | 1.8 | 1.7 |
| Efficiency (%) | 96.2 | 96 | 95.4 |
| Power density (W/cm ³) | 8.38 | 8.35 | 6.66 |
| Torque ripple (%) | 35 | 120 | 92 |

6. Conclusions

In this study, a detailed design, analysis and optimization of a high power density rotor segmented DSAFSRM were performed. A hybrid design algorithm based on non-linear MEC and classical formulations was proposed, showing simplicity and acceptable accuracy at the same time. In order to minimize the unacceptably high torque ripple of the DSAFSRM, a two-step optimization procedure was introduced, which reduced the torque ripple from 120% to 35% while increasing the efficiency by up to 96.2%. Moreover, a double-sided radial flux SRM was designed and compared with the optimized and initial DSAFSRM. The results showed that the optimized DSAFSRM offered roughly 26% and 0.8% higher output power and efficiency, respectively, than the double-sided radial flux SRM. In addition, the DSAFSRM possessed a significantly superior torque profile with respect to its radial flux counterpart, with 57% less torque ripple and 65 N m higher average torque.

Author Contributions: Conceptualization, methodology, formal analysis, investigation, writing—original draft preparation and visualization, A.M.A.; Writing—review and editing, supervision, M.N.I. and P.S. All authors have read and agreed to the published version of the manuscript.

Funding: This research was supported by Marie-Curie-Doctoral-Industrial project (HORIZON-MSCA-2021-DN-01) with the title “New Generation of Electrical Machines Enabled by Additive Manufacturing—EMByAM” and Research Foundation—Flanders (FWO) in the project (S001721N) entitled “Multi-Material Additive Manufacturing for Electrical Machines with increased performance (AM4EM)”.

Data Availability Statement: Not applicable.

Conflicts of Interest: The authors declare no conflict of interest.

Appendix A

The expanded form of (21) is as follows.

$$\begin{bmatrix} G_{t1} + 2G_{y1} & -2G_{y1} & 0 & 0 & 0 & 0 \\ -2G_{y1} & 2(G_{y1} + G_{y2} + G_{t2}) & -2G_{y2} & 0 & -2G_{t2} & 0 \\ 0 & -2G_{y2} & 4G_{y3} + 2G_{y2} + 2G_{t3} & -4G_{y3} & 0 & -2G_{t3} \\ 0 & 0 & -4G_{y3} & 4G_{y3} + 2G_s + G_m & 0 & -2G_s \\ 0 & -2G_{t2} & 0 & 0 & 2(G_s + G_{sc} + G_{t2}) & -2G_s \\ 0 & 0 & -2G_{t3} & -2G_s & -2G_s & 4G_s + 2G_{t3} \end{bmatrix} \begin{bmatrix} V_1 \\ V_2 \\ V_3 \\ V_4 \\ V_5 \\ V_6 \end{bmatrix} = \begin{bmatrix} -N_c I_a G_{t1} \\ 0 \\ 0 \\ 0 \\ 0 \\ 0 \end{bmatrix} \quad (A1)$$

where G_m has different values in the aligned and non-aligned positions as in (A2) and (A3), respectively.

$$G_m = \frac{2G_{ry1}G_{g1,1}^{aligned}}{2G_{ry1} + G_{g1,1}^{aligned}} \quad (A2)$$

$$G_m = \frac{4G_{ry1}G_{g1,1}^{unaligned}}{2G_{ry1} + G_{g1,1}^{unaligned}} + 2G_{ss} \quad (A3)$$

References

- Xu, Z.; Li, T.; Zhang, F.; Wang, H.; Dee, J.; Ahn, J.-W. Characteristics Evaluation of a Segmental Rotor Type Switched Reluctance Motor with Concentrated Winding for Torque Density and Efficiency Improvement. *Energies* **2022**, *15*, 8915. [\[CrossRef\]](#)
- Andriushchenko, E.; Kallaste, A.; Mohammadi, M.H.; Lowther, D.A.; Heidari, H. Sensitivity Analysis for Multi-Objective Optimization of Switched Reluctance Motors. *Machines* **2022**, *10*, 559. [\[CrossRef\]](#)
- Diao, K.; Sun, X.; Lei, G.; Guo, Y.; Zhu, J. Multimode optimization of switched reluctance machines in hybrid electric vehicles. *IEEE Trans. Energy Convers.* **2020**, *36*, 2217–2226. [\[CrossRef\]](#)
- Terzić, M.V.; Mihić, D.S. Switched Reluctance Motor Design for a Mid-Drive E-Bike Application. *Machines* **2022**, *10*, 642. [\[CrossRef\]](#)
- Wattewarduge, G.; Bilgin, B. Sizing of the Motor Geometry for an Electric Aircraft Propulsion Switched Reluctance Machine Using a Reluctance Mesh-Based Magnetic Equivalent Circuit. *Machines* **2023**, *11*, 59. [\[CrossRef\]](#)
- Zine, M.; Chems, A.; Labiod, C.; Ikhlef, M.; Srairi, K.; Benbouzid, M. Coupled indirect torque control and maximum power point tracking technique for optimal performance of 12/8 switched reluctance generator-based wind turbines. *Machines* **2022**, *10*, 1046. [\[CrossRef\]](#)
- Xu, Z.; Li, T.; Zhang, F.; Zhang, Y.; Lee, D.-H.; Ahn, J.-W. A Review on Segmented Switched Reluctance Motors. *Energies* **2022**, *15*, 9212. [\[CrossRef\]](#)
- Ghaheri, A.; Naghash, R.; Ajamloo, A.M.; Afjei, E. Design Comparison of BLDC and SR Motor Drives for Range Hood Applications. In Proceedings of the 2021 29th Iranian Conference on Electrical Engineering (ICEE), Tehran, Iran, 18–20 May 2021; pp. 220–225.
- Nasiri-Zarandi, R.; Ajamloo, A.M. Implementation of PM step skew technique to optimum design of a transverse flux PM generator for small scale wind turbine. In Proceedings of the 2019 IEEE Milan PowerTech, Milan, Italy, 23–27 June 2019; pp. 1–6.
- Lukman, G.F.; Nguyen, X.S.; Ahn, J.-W. Design of a low torque ripple three-phase SRM for automotive shift-by-wire actuator. *Energies* **2020**, *13*, 2329. [\[CrossRef\]](#)
- Lan, Y.; Frikha, M.A.; Croonen, J.; Benômar, Y.; El Baghdadi, M.; Hegazy, O. Design Optimization of a Switched Reluctance Machine with an Improved Segmental Rotor for Electric Vehicle Applications. *Energies* **2022**, *15*, 5772. [\[CrossRef\]](#)
- Garcia-Amorós, J.; Marín-Genescà, M.; Andrada, P.; Martínez-Piera, E. Two-phase linear hybrid reluctance actuator with low detent force. *Energies* **2020**, *13*, 5162. [\[CrossRef\]](#)
- Gupta, T.D.; Chaudhary, K.; Elavarasan, R.M.; Saket, R.; Khan, I.; Hossain, E. Design modification in single-tooth winding double-stator switched reluctance motor for torque ripple mitigation. *IEEE Access* **2021**, *9*, 19078–19096. [\[CrossRef\]](#)
- Zhao, G.; Hua, W.; Qi, J. Comparative study of wound-field flux-switching machines and switched reluctance machines. *IEEE Trans. Ind. Appl.* **2019**, *55*, 2581–2591. [\[CrossRef\]](#)
- Ajamloo, A.M.; Ghaheri, A.; Nasiri-Zarandi, R. Design and Optimization of a New TFPM Generator with Improved Torque Profile. In Proceedings of the 2019 International Power System Conference (PSC), Tehran, Iran, 9–11 December 2019; pp. 106–112.
- Gundogmus, O.; Elamin, M.; Yasa, Y.; Husain, T.; Sozer, Y.; Kutz, J.; Tylenda, J.; Wright, R.L. Acoustic noise mitigation of switched reluctance machines with windows on stator and rotor poles. *IEEE Trans. Ind. Appl.* **2020**, *56*, 3719–3730. [\[CrossRef\]](#)
- Lukman, G.F.; Ahn, J.-W. Torque ripple reduction of switched reluctance motor with non-uniform air-gap and a rotor hole. *Machines* **2021**, *9*, 348. [\[CrossRef\]](#)
- Azer, P.; Bilgin, B.; Emadi, A. Comprehensive analysis and optimized control of torque ripple and power factor in a three-phase mutually coupled switched reluctance motor with sinusoidal current excitation. *IEEE Trans. Power Electron.* **2020**, *36*, 7150–7164. [\[CrossRef\]](#)
- Wang, J.; Jiang, W.; Wang, S.; Lu, J.; Williams, B.W.; Wang, Q. A novel step current excitation control method to reduce the torque ripple of outer-rotor switched reluctance motors. *Energies* **2022**, *15*, 2852. [\[CrossRef\]](#)
- Li, H.; Bilgin, B.; Emadi, A. An improved torque sharing function for torque ripple reduction in switched reluctance machines. *IEEE Trans. Power Electron.* **2018**, *34*, 1635–1644. [\[CrossRef\]](#)
- Sun, X.; Wu, J.; Lei, G.; Guo, Y.; Zhu, J. Torque ripple reduction of SRM drive using improved direct torque control with sliding mode controller and observer. *IEEE Trans. Ind. Electron.* **2020**, *68*, 9334–9345. [\[CrossRef\]](#)
- Kawa, M.; Kiyota, K.; Furqani, J.; Chiba, A. Acoustic noise reduction of a high-efficiency switched reluctance motor for hybrid electric vehicles with novel current waveform. *IEEE Trans. Ind. Appl.* **2018**, *55*, 2519–2528. [\[CrossRef\]](#)
- Jing, B.; Dang, X.; Liu, Z.; Ji, J. Torque Ripple Suppression of Switched Reluctance Motor with Reference Torque Online Correction. *Machines* **2023**, *11*, 179. [\[CrossRef\]](#)
- Zhu, J.; Cheng, K.W.E.; Xue, X. Design and analysis of a new enhanced torque hybrid switched reluctance motor. *IEEE Trans. Energy Convers.* **2018**, *33*, 1965–1977. [\[CrossRef\]](#)
- Kondelaji, M.A.J.; Farahani, E.F.; Mirsalim, M. Performance analysis of a new switched reluctance motor with two sets of embedded permanent magnets. *IEEE Trans. Energy Convers.* **2020**, *35*, 818–827. [\[CrossRef\]](#)

26. Ding, W.; Yang, S.; Hu, Y.; Li, S.; Wang, T.; Yin, Z. Design consideration and evaluation of a 12/8 high-torque modular-stator hybrid excitation switched reluctance machine for EV applications. *IEEE Trans. Ind. Electron.* **2017**, *64*, 9221–9232. [[CrossRef](#)]
27. Yan, W.; Chen, H.; Liao, S.; Liu, Y.; Cheng, H. Design of a low-ripple double-modular-stator switched reluctance machine for electric vehicle applications. *IEEE Trans. Transp. Electrification*. **2021**, *7*, 1349–1358. [[CrossRef](#)]
28. Cheng, H.; Liao, S.; Yan, W. Development and performance analysis of segmented-double-stator switched reluctance machine. *IEEE Trans. Ind. Electron.* **2021**, *69*, 1298–1309. [[CrossRef](#)]
29. Ghaffarpour, A.; Mirsalim, M. Split-tooth double-rotor permanent magnet switched reluctance motor. *IEEE Trans. Transp. Electrification*. **2022**, *8*, 2400–2411. [[CrossRef](#)]
30. Torkaman, H.; Ghaheri, A.; Keyhani, A. Axial flux switched reluctance machines: A comprehensive review of design and topologies. *IET Electr. Power Appl.* **2019**, *13*, 310–321. [[CrossRef](#)]
31. Madhavan, R.; Fernandes, B. A novel axial flux segmented SRM for electric vehicle application. In Proceedings of the XIX International Conference on Electrical Machines-ICEM 2010, Rome, Italy, 6–8 September 2010; pp. 1–6.
32. Madhavan, R.; Fernandes, B.G. Axial flux segmented SRM with a higher number of rotor segments for electric vehicles. *IEEE Trans. Energy Convers.* **2013**, *28*, 203–213. [[CrossRef](#)]
33. Yu, F.; Chen, H.; Yan, W.; Pires, V.F.; Martins, J.F.; Rafajdus, P.; Musolino, A.; Sani, L.; Aguirre, M.P.; Saqib, M.A. Design and Multiobjective Optimization of A Double-stator Axial Flux SRM with Full-pitch Winding Configuration. *IEEE Trans. Transp. Electrification*. **2022**, *8*, 4348–4364. [[CrossRef](#)]
34. Ma, J.; Qu, R.; Li, J. Optimal design of axial flux switched reluctance motor for electric vehicle application. In Proceedings of the 2014 17th International Conference on Electrical Machines and Systems (ICEMS), Hangzhou, China, 22–25 October 2014; pp. 1860–1865.
35. Labak, A.; Kar, N.C. Designing and prototyping a novel five-phase pancake-shaped axial-flux SRM for electric vehicle application through dynamic FEA incorporating flux-tube modeling. *IEEE Trans. Ind. Appl.* **2013**, *49*, 1276–1288. [[CrossRef](#)]
36. Labak, A.; Kar, N.C. A novel five-phase pancake shaped switched reluctance motor for hybrid electric vehicles. In Proceedings of the 2009 IEEE Vehicle Power and Propulsion Conference, Dearborn, MI, USA, 7–11 September 2009; pp. 494–499.
37. Andrada, P.; Blanqué, B.; Martínez, E.; Perat, J.I.; Sánchez, J.A.; Torrent, M. Design of a novel modular axial-flux double rotor switched reluctance drive. *Energies* **2020**, *13*, 1161. [[CrossRef](#)]
38. Teixeira, V.S.D.C.; Barros, T.A.D.S.; Moreira, A.B.; Ruppert Filho, E. Methodology for the electromagnetic design of the axial-flux C-core switched reluctance generator. *IEEE Access* **2018**, *6*, 65463–65473. [[CrossRef](#)]
39. Ma, J.; Li, J.; Fang, H.; Li, Z.; Liang, Z.; Fu, Z.; Xiao, L.; Qu, R. Optimal design of an axial-flux switched reluctance motor with grain-oriented electrical steel. *IEEE Trans. Ind. Appl.* **2017**, *53*, 5327–5337. [[CrossRef](#)]
40. Sun, W.; Li, Q.; Liu, K.; Li, L. Design and analysis of a novel rotor-segmented axial-field switched reluctance machine. *CES Trans. Electr. Mach. Syst.* **2017**, *1*, 238–245. [[CrossRef](#)]
41. Sun, W.; Li, Q.; Sun, L.; Li, L. Development and investigation of novel axial-field dual-rotor segmented switched reluctance machine. *IEEE Trans. Transp. Electrification*. **2020**, *7*, 754–765. [[CrossRef](#)]
42. Krishnan, R. *Switched Reluctance Motor Drives: Modeling, Simulation, Analysis, Design, and Applications*; CRC Press: Boca Raton, FL, USA, 2017.
43. Gieras, J.F. *Permanent Magnet Motor Technology: Design and Applications*; CRC Press: Boca Raton, FL, USA, 2009.
44. Ostovic, V. *Dynamics of Saturated Electric Machines*; Springer Science & Business Media: Berlin/Heidelberg, Germany, 2012.

Disclaimer/Publisher’s Note: The statements, opinions and data contained in all publications are solely those of the individual author(s) and contributor(s) and not of MDPI and/or the editor(s). MDPI and/or the editor(s) disclaim responsibility for any injury to people or property resulting from any ideas, methods, instructions or products referred to in the content.